

# Multi-sensors study of precipitable water vapour over mainland China

Man Sing Wong,<sup>a\*</sup> Xiaomeng Jin,<sup>b</sup> Zhizhao Liu,<sup>a</sup> Janet Nichol<sup>a</sup> and P. W. Chan<sup>c</sup>

<sup>a</sup> Department of Land Surveying and Geo-Informatics, The Hong Kong Polytechnic University, Kowloon, Hong Kong

<sup>b</sup> Center for Sustainability and Global Environment, Nelson Institute for Environmental Studies, University of Wisconsin-Madison, WI, USA

<sup>c</sup> Hong Kong Observatory, Hong Kong

**ABSTRACT:** Water vapour, an important greenhouse gas in the atmosphere, is crucial for hydrological, atmospheric, and meteorological processes. This study first compared five precipitable water vapour (PWV) products from multi-sensors including radiosonde, AERosol RObotic NETwork (AERONET) sunphotometer, Global Positioning System (GPS) and MODerate resolution Imaging Spectroradiometer (MODIS), and then characterized the spatial and temporal trends of PWV in mainland China. Intercomparison results indicate good agreements among PWV products with correlation coefficients ranging from 0.775 to 0.937. As for spatial analysis, 13 years of MODIS MOD05 products were investigated and the spatial distribution of PWV is closely correlated with the topography, e.g. latitude and altitude, in mainland China. A monotonically increasing annual trend was detected in some radiosonde sites in China between 1976 and 1999, but a decreasing trend was observed between 2000 and 2012. Analysis of the differences in PWV between weekdays and weekends indicated a marked weekend effect, suggesting the influence of anthropogenic activities. Diurnal variations in PWV were also studied from 1999 to 2009 using GPS data. A pronounced diurnal cycle of PWV was observed in most of the sites during summer and spring seasons.

KEY WORDS AERONET; GPS; MODIS; precipitable water vapour; radiosonde

Received 13 January 2014; Revised 30 September 2014; Accepted 10 October 2014

## 1. Introduction

Atmospheric water vapour plays an important role in hydrological processes, atmospheric circulation, and weather systems. Water vapour is the primary greenhouse gas whose radiative effects may amplify the response of climate, leading to further global warming (Raval and Ramanathan, 1989; Held and Soden, 2000). In addition, water vapour itself is an essential component in the atmosphere that is closely related to surface evaporation, cloud formation, precipitation, and circulation transportation (Starr and Melfi, 1991; Fontaine *et al.*, 2003). Despite its importance, accurate and timely measurements of water vapour distribution are challenging due to its high spatial and temporal variability as well as its interactions with global warming and anthropogenic activities (Liu *et al.*, 2012).

Radiosonde is the most common instrument to measure atmospheric water vapour contents, and has provided data worldwide for over half a century (Gaffen *et al.*, 1991). Given its high accuracy and high vertical resolution, radiosonde water vapour data are often used as reference data to evaluate other water vapour measuring techniques (Soden and Lanzante, 1996; Brettle and Galvin, 2003).

However, limitations such as unevenly spaced observation stations, expensive, and uncontrollable balloon prohibit the usability of radiosonde for water vapour monitoring over large areas. In addition, the low temporal resolution of radiosonde cannot track the temporal variations of water vapour contents between sampling intervals (Van Baelen *et al.*, 2005).

Satellite observations have been used for two decades to provide a synoptic view of water vapour distribution and are increasingly gaining interest due to the rapid development of remote sensing techniques (King *et al.*, 1992). Among multiple sensors, MODerate resolution Imaging Spectroradiometer (MODIS), on board NASA's TERRA and AQUA space platforms, is the most widely used sensor for water vapour retrieval. Several studies have confirmed the value of MODIS products (MOD05 and MOD07) for global monitoring of water vapour column concentrations (King *et al.*, 1992; Gao and Kaufman, 2003).

Global positioning systems (GPS) are able to estimate the atmospheric propagation delay and further compute the atmospheric water vapour column (Bevis *et al.*, 1992). Given the increase in the number of operational GPS receivers and mature positioning techniques, GPS meteorology has attracted much attention recently due to its high level of accuracy (Elgered *et al.*, 1997; Emardson *et al.*, 1998), high temporal resolution, relatively low cost, and all weather measurements (Hernández-Pajares *et al.*, 2001; Bokoye *et al.*, 2003). Moreover, GPS slant observation can provide three-dimensional water vapour structure

\* Correspondence to: M. S. Wong, Department of Land Surveying and Geo-Informatics, The Hong Kong Polytechnic University, Hung Hom, Kowloon, Hong Kong. E-mail: lswong@polyu.edu.hk

in the atmosphere, which can complement the limitation of remote sensing satellite observations that only measure integrated vertical column (Song *et al.*, 2006).

Sunphotometers, which operate at the 940 nm wavelength of strong water vapour absorption, have been used to estimate water vapour column abundance (Schmid *et al.*, 1996; Halthore *et al.*, 1997). NASA's AErosol RObotic NETwork (AERONET), consisting of over 300 sunphotometers worldwide, provides standardized water vapour data with high frequency. The merits of AERONET sunphotometers include low maintenance cost, real-time data collection, and high level of accuracy (Holben *et al.*, 1998; Mätzler *et al.*, 2002; Bokoye *et al.*, 2003). Sunphotometers have been recognized for capturing the short-term variability of water vapour contents, such as rainfall forecasting (Liu *et al.*, 2012).

As a result of diverse topography and the influence of monsoon, the distribution of water vapour in mainland China varies in space and time. The availability of multi-sensor data has facilitated the study of water vapour as an important component in the hydrological cycle. Bi *et al.* (2004) estimated the integrated water vapour column from GPS data at three stations in the southwest China and demonstrated its high level of accuracy with reference to radiosonde data and National Centers for Environmental Prediction (NCEP) reanalysis data. To understand the long-term dynamics of water vapour, radiosonde data have been used for annual and seasonal variation analysis, which are usually correlated with surface temperature, altitude, latitude, monsoon, and precipitation (Zhai and Eskridge, 1997; Wang and Chen, 2012; Zhao *et al.*, 2012). GPS water vapour data are widely studied for short time span analysis, such as diurnal variation and weather forecasting (Song *et al.*, 2006; Jin *et al.*, 2008). However, most studies in China remain at the stage of case studies for a specific area or using a single data set. Instead, this paper examined the spatial and temporal variations of precipitable water vapour (PWV) distribution over the entire Chinese Mainland by integrating data sets from multi-sensors, including radiosonde, GPS, MODIS MOD05, MODIS MOD07, and AERONET sunphotometers. Thoroughly understanding the characteristics of water vapour distributions is crucial in hydrological and climatic processes, as well as its relationship with anthropogenic activities.

In our study, PWV refers to an integrated vertical water vapour column in the atmosphere. The main objectives of this paper are: (1) to compare five PWV products from multi-sensors including radiosonde, AERONET sunphotometer, GPS, and MODIS; (2) to characterize the spatial variations of PWV in mainland China; and (3) to analyse the long-term, weekend effect and the diurnal cycle of PWV in mainland China.

## 2. Study area

China is located in the east Asia between latitudes 18°N and 54°N, and longitudes 73°E and 135°E, with a territory

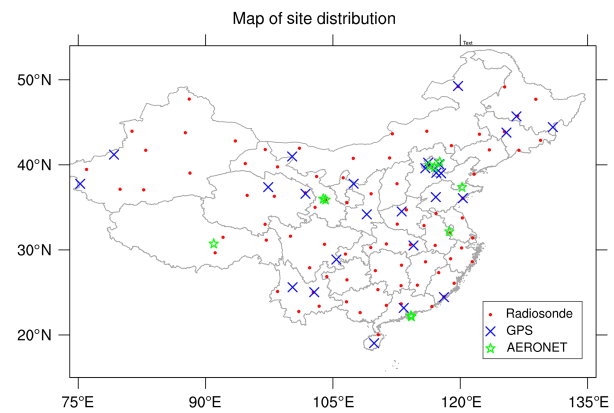


Figure 1. Spatial distribution of radiosonde, GPS, and AERONET sunphotometer stations in mainland China.

of over 9.7 million km<sup>2</sup> and a population of 1.339 billion (China Census Data, 2010). The topography in China can be characterized as mountainous in the west and flat plains in the east. The Asian monsoon brings distinct seasonal variations, with cold, dry winters and wet, hot summers to China. Because of rapid urbanization and excessive resource exploitation, China has experienced observable climate changes over the last century: characterized by a warming trend especially in northern China, increasing rainfall contrast between northern and southern China, as well as more frequent droughts and floods (Piao *et al.*, 2010). As an important parameter for the analysis of weather systems, PWV distribution in China displays high spatial and temporal variations that are closely correlated with topography, surface temperature, and the monsoon (Zhai and Eskridge, 1997). In this study, PWV data from 83 radiosonde stations, 26 GPS stations, and 10 AERONET sunphotometer stations in mainland China were used (Figure 1).

## 3. Data acquisition and processing

Table 1 summarizes the characteristics of data used in this study in terms of time span, temporal sampling, spatial resolution, derivation method, and retrieval accuracy.

### 3.1. Radiosonde data

Based on the balloon-borne platform, radiosonde can directly measure the meteorological parameters such as atmospheric pressure, temperature, and relative humidity at different altitudes. The ascent rate of the balloon is usually in the range of 5–8 m s<sup>-1</sup> (World Meteorological Organization, 2008). A radiosonde includes electronic subsystems that record samples at regular intervals (e.g. every 2–5 s) and transmit the data to a ground-based receiver and data acquisition system. Thus, the radiosonde has observations with a vertical resolution of 10–40 m. Several factors, including dry bias, time-lag error, and calibration reference drift, may influence the accuracy of radiosonde (Turner *et al.*, 2003; Miloshevich *et al.*, 2006; Pérez-Ramírez *et al.*, 2014). The uncertainty of radiosonde

Table 1. Summary of data characteristics.

Data source	Time span	Temporal sampling	Spatial resolution	Derivation method	Estimated uncertainty	Weather limitation
Radiosonde	1976–2012	0000 UTC and 1200 UTC time	83 sites, point measurement	Radio telemetry (Brette and Galvin, 2003)	5–8% (Pérez-Ramírez <i>et al.</i> , 2014)	No
AERONET Sunphotometer	2001–2012	15-min during daytime	10 sites, point measurement	Sunphotometer (Reagan <i>et al.</i> , 1992)	10% (Alexandrov <i>et al.</i> , 2009)	Clear sky and rain-free
GPS	1999–2009	Every 1 h, all day, all weather	26 sites, point measurement	ZWD estimation (Bevis <i>et al.</i> , 1992)	5–7% (Miloshevich <i>et al.</i> , 2006)	No
MOD05_L2	2000–2012	Every day	1 km	Near infrared water vapour; retrieval algorithm (Kaufman and Gao, 1992)	5–10% (Gao and Kaufman, 2003)	Clear sky only
MOD07_L2	2000–2012	Every day and night	5 km	Near infrared water vapour; retrieval algorithm (Seemann <i>et al.</i> , 2006)	10% (Seemann <i>et al.</i> , 2006)	Clear sky only

PWV data has been reported from 5 to 8% (Turner *et al.*, 2003; Pérez-Ramírez *et al.*, 2014).

Radiosonde data from 1976 to 2012 were used in this study. Radiosonde is launched twice daily at 0000 UTC and 1200 UTC. The PWV column abundance can be calculated using Equation (1) (Liu *et al.*, 2012):

$$W = \frac{1}{g} \int_{p_1}^{p_2} x \, dp \quad (1)$$

where  $W$  is the vertically integrated water vapour column (unit: mm) within a layer;  $p_1$  and  $p_2$  are atmospheric pressures (unit: Pascal) at the layer's upper and lower boundaries;  $g$  is the acceleration of gravity ( $9.806 \text{ ms}^{-2}$  used in this study);  $x$  is the mixing ratio (unit:  $\text{g kg}^{-1}$ ), which can be obtained from Equation (2):

$$x = \frac{0.622 \cdot e}{p - e} \quad (2)$$

where  $p$  is the pressure (unit: Pascal);  $e$  is the vapour pressure (unit: Pascal) that can be derived from  $e = \text{RH} \cdot e_s(T)$ , RH is the relative humidity (unit: %) of the atmosphere and  $e_s$  is the saturation vapour pressure (unit: Pascal) that is a function of temperature (unit:  $^{\circ}\text{C}$ ).

### 3.2. AERONET sunphotometer data

AERONET is a network of sunphotometers established by NASA and expanded by international collaboration, and its main purpose is to monitor aerosol optical and microphysical characteristics worldwide (Holben *et al.*, 1998). AERONET provides PWV data together with aerosol optical properties. Typically, AERONET provides data at three levels, namely level 1.0 (unscreened), level 1.5 (cloud-screened), and level 2.0 (cloud screened and quality-assured). In this study, level 2.0 data from 10 AERONET sunphotometer stations in China were acquired. Estimation of the PWV column is based on the modified Langley algorithm, in which the spectral transmission of solar irradiance at 940 nm is measured by

sunphotometers (Bokoye *et al.*, 2007), and it is expressed as in Equation (3):

$$\text{PWV} = \frac{1}{m} \left( \frac{1}{a} \left( \ln \left( \frac{V_0(\lambda) \cdot R^{-2}}{V(\lambda)} \right) - m_r \cdot \tau_r(\lambda) - m \cdot \tau_a(\lambda) \right) \right)^{1/b} \quad (3)$$

where PWV (unit: cm) is the estimated PWV column;  $m$  (unit: kg) is the air mass;  $a$  and  $b$  are constants that can be observed from curve-fitting procedure (Schmid *et al.*, 1996);  $V_0(\lambda)$  is a constant that can be determined from sunphotometer;  $V(\lambda)$  is the output from sunphotometer;  $R$  is the Earth–Sun distance (in astronomical units) at the time of observation;  $m_r$  (unit: kg) is the pressure-corrected air mass;  $\tau_r(\lambda)$  is the Rayleigh optical thickness; and  $\tau_a(\lambda)$  is the aerosol optical thickness at 940 nm. Signal noise and uncertainty associated with calibration process may induce a systematic uncertainty of PWV with 4–5% (Pérez-Ramírez *et al.*, 2014). In addition, the derivation of coefficients  $a$  and  $b$  in Equation (3) is influenced by temperature, pressure, and humidity, leading to 5% quantification uncertainty (Alexandrov *et al.*, 2009). Thus, the combined uncertainty of sunphotometer PWV is around 10% (Alexandrov *et al.*, 2009; Pérez-Ramírez *et al.*, 2014).

### 3.3. GPS data

GPS techniques have successfully demonstrated the ability to retrieve PWV at a high temporal resolution (e.g. 10 or 30 min). Several studies have derived water vapour from GPS data, and the difference between water vapour derived from GPS and radiosonde is approximately 1–2 mm (Elgered *et al.*, 1997; Tregoning *et al.*, 1998; Niell *et al.*, 2001; Li, 2003). Modelling errors and the uncertainties associated with mapping functions may induce a combined uncertainty of GPS PWV data at 5–7% (Bevis *et al.*, 1992; Pérez-Ramírez *et al.*, 2014).

In this study, PWV data from the ground-based GPS meteorological network at 26 stations in China were derived. GPS signals have a range delay when they propagate through the troposphere. The zenith tropospheric delay (ZTD), a range delay mapped to the zenith direction of the GPS station, can usually be estimated as a parameter together with GPS receiver coordinates (Collins *et al.*, 2002). This ZTD is usually decomposed into two components: zenith hydrostatic delay (ZHD) and zenith wet delay (ZWD). The ZWD is proportional to the amount of integrated water vapour (Bokoye *et al.*, 2003). Compared with ZWD modelling, the ZHD can be constructed from an empirical model with much higher precision. Thus the ZWD is usually obtained by subtracting ZHD from ZTD. The ZHD can be calculated using Equation (4) (Iwabuchi *et al.*, 2000):

$$\text{ZHD} = (2.2997 \pm 0.0024) \frac{P_s}{f(\varphi, H)} \quad (4)$$

with

$$f(\varphi, H) = 1 - 0.00266 \cos 2\varphi - 0.00028H \quad (5)$$

where  $P_s$  is the atmospheric pressure (unit: hPa), and  $\varphi$  and  $H$  are the latitude and height (unit: m) of GPS site. Then, ZWD can be calculated using Equation (6):

$$\text{ZWD} = \text{ZTD} - \text{ZHD} \quad (6)$$

Finally, PWV can be calculated using Equation (7):

$$\text{PWV} = \Pi \cdot \text{ZWD} \quad (7)$$

where  $\Pi$  is a constant value that is relevant to weighted mean atmospheric temperature (Bevis *et al.*, 1992).

### 3.4. MODIS data

MODIS is a remote scanning spectroradiometer with 36 bands between 0.645 and 14.235 μm (King *et al.*, 1992). MODIS level 2 collection 5 operational PWV products, namely MOD05 and MOD07, were acquired from the NASA Goddard Earth Science Distributed Active Archive Center (DAAC). Near-infrared water vapour algorithm was applied to MOD05 products, while infrared water vapour algorithm was applied to MOD07 products. MOD05 and MOD07 PWV products have 1 and 5 km spatial resolution, respectively.

The MODIS near infrared water vapour products (MOD05) estimate water vapour column over clear areas of the globe (Gao and Kaufman, 1998). The differential absorption technique is employed in the PWV retrieval algorithm of MOD05 products. The PWV column is derived from the comparison between the reflected solar radiation in the absorption channels centred near 0.905, 0.936, and 0.94 μm and that in nearby non-absorption channels centred at 0.865 and 1.240 μm (Gao and Kaufman, 1998). Sources of errors for PWV retrieval include the uncertainties in surface reflectance, sensor calibration, spectral response uncertainty, geometric registration, atmospheric profiles, and the effect of haze (Gao and

Kaufman, 2003). Typical uncertainty of MODIS products range from 5 to 10% (Gao and Kaufman, 2003).

Moisture profile of MOD07 is derived from three infrared bands centred at 9.730, 7.325, and 8.550 μm, respectively. The total column of PWV is calculated by integrating the 101-level mixing ratio profiles (Seemann *et al.*, 2006). The statistical synthetic regression method is employed for PWV retrieval, and the subsequent non-linear physical retrieval is added as optional (Menzel and Gumley, 1996). The retrieval of PWV is performed by averaging the radiance of clear pixels over the 5 × 5 km<sup>2</sup> areas. Sources of uncertainty include surface reflectance, calibration error, spectral response uncertainty, profile inaccuracy, and forward model error. The overall uncertainty of MOD07 is around 10% (Seemann *et al.*, 2006).

## 4. Comparison between AERONET sunphotometer, GPS, MODIS, and radiosonde data

### 4.1. Statistical metrics

Radiosonde data have been confirmed to have high level of PWV accuracy (Soden and Lanzante, 1996; Brettle and Galvin, 2003), and in this study, they were used as a reference to compare with PWV retrieved from AERONET sunphotometer, GPS, and MODIS products. Spatial and temporal collocation was conducted with the following methods. First, to obtain sufficient data pairs and reduce the impacts caused by spatial discrepancies between stations, the collocation of ground station measurements was conducted with less than half-degree in both latitude and longitude. In addition, as the temporal resolutions of PWV products are different (Table 1). AERONET sunphotometer data, which has the finest temporal resolution with ~15 min, were averaged to 1 h for comparing with radiosonde and MODIS products. As the time lag between MODIS and radiosonde is longer than 1 h, radiosonde data with the least time lag were chosen for comparing with MODIS data.

Four statistical metrics were used to evaluate the retrieval performance, including root mean square error (RMSE), mean bias (MB), correlation coefficient ( $R^2$ ), and index of agreement ( $d$ ) (Willmott, 1981). The root mean square error (RMSE), which is defined in Equation (8), is used for quantifying the differences between paired data sets:

$$\text{RMSE} = \sqrt{\frac{\sum_{i=1}^n (\text{PWV}_{o_i} - \text{PWV}_{R_i})^2}{n}} \quad (8)$$

where  $n$  is the number of data pairs;  $\text{PWV}_{o_i}$  is the observed PWV column;  $\text{PWV}_{R_i}$  is the reference PWV column.

The mean bias (MB) provides information on the over-estimation/underestimation of each data set, which can be defined as Equation (9):

$$\text{MB} = \frac{1}{n} \sum_{i=1}^n (\text{PWV}_{o_i} - \text{PWV}_{R_i}) \quad (9)$$

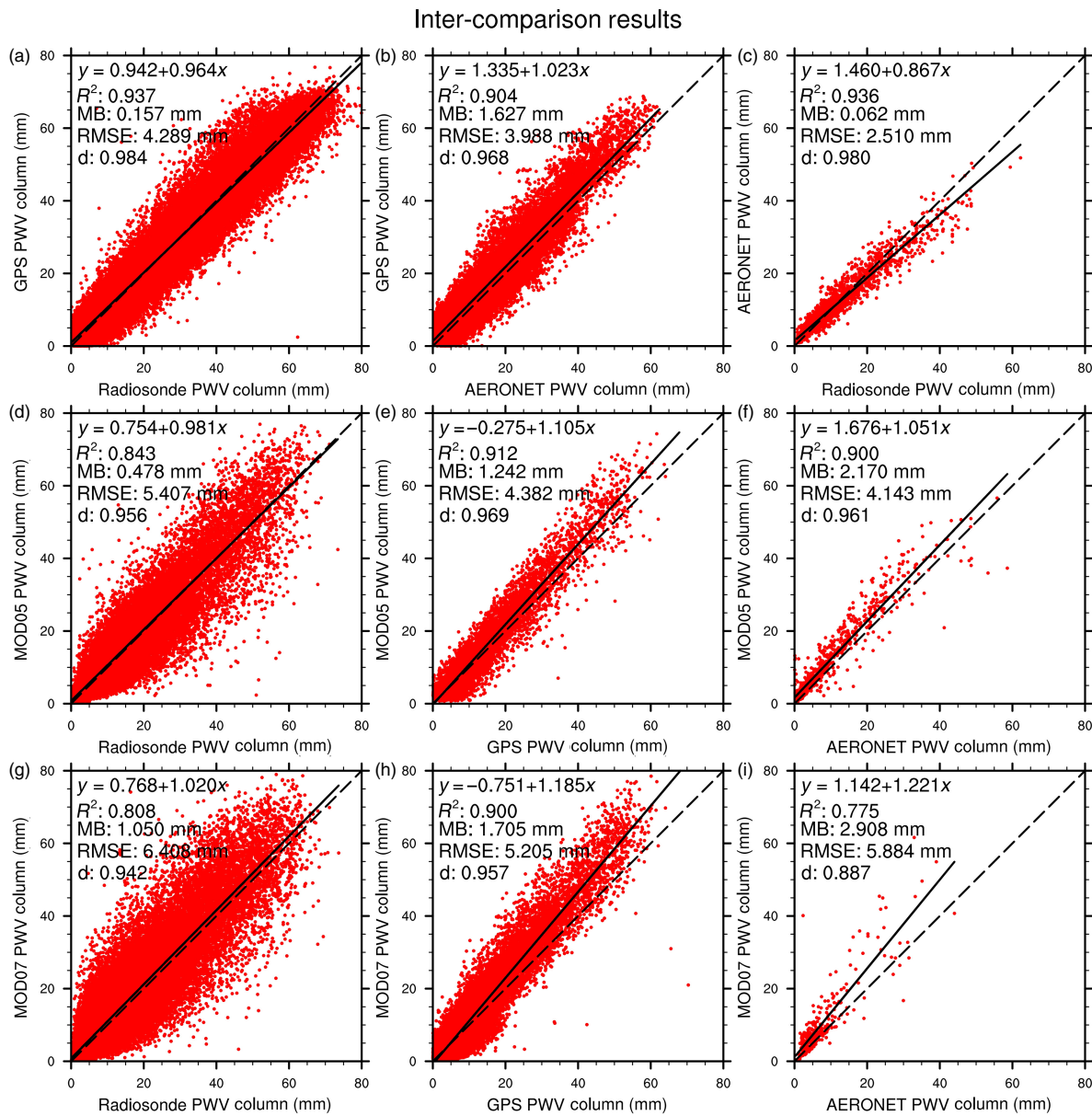


Figure 2. Comparison between (a) GPS versus radiosonde; (b) GPS versus AERONET sunphotometer; (c) AERONET sunphotometer versus radiosonde; (d) MODIS MOD05 versus radiosonde; (e) MODIS MOD05 versus AERONET sunphotometer; (f) MODIS MOD07 versus radiosonde; (g) MODIS MOD07 versus GPS; and (h) MODIS MOD07 versus AERONET sunphotometer.

The correlation coefficient ( $R^2$ ) indicates the strength of linear relationship between paired data sets, which is calculated as the square of Pearson product (Equation (10)):

$$R = \frac{\left[ \sum_{i=1}^n (\text{PWV}_{\text{o}_i} - \overline{\text{PWV}}_{\text{o}})(\text{PWV}_{\text{R}_i} - \overline{\text{PWV}}_{\text{R}}) \right]}{\sqrt{\sum_{i=1}^n (\text{PWV}_{\text{o}_i} - \overline{\text{PWV}}_{\text{o}})^2 \sum_{i=1}^n (\text{PWV}_{\text{R}_i} - \overline{\text{PWV}}_{\text{R}})^2}} \quad (10)$$

where  $\overline{\text{PWV}}_{\text{o}}$  and  $\overline{\text{PWV}}_{\text{R}}$  indicate the average values of observed and reference PWV.

The index of agreement ( $d$ ) provides a standardized measure that ranges from 0 to 1 (Willmott, 1981), to quantify the estimated differences between  $\text{PWV}_{\text{o}}$  and

$\text{PWV}_{\text{R}}$ , which can be defined as Equation (11):

$$d = 1 - \frac{n \cdot \text{RMSE}^2}{\sum_{i=1}^n \left( |\text{PWV}_{\text{o}_i} - \overline{\text{PWV}}_{\text{o}}| + |\text{PWV}_{\text{R}_i} - \overline{\text{PWV}}_{\text{R}}| \right)^2} \quad (11)$$

#### 4.2. Intercomparisons among GPS, radiosonde, and AERONET sunphotometer

GPS PWV data with hourly temporal resolution were compared with radiosonde and AERONET sunphotometer data, respectively. Sixteen GPS and radiosonde collocated stations were identified and a total of 78,226 pairs of data were selected. The GPS PWV data agree well with radiosonde PWV data ( $R^2 = 0.937$ ,  $d = 0.984$ ), although

Table 2. Statistical summary of comparison results (scatterplots of comparison results can be referred to Figure 2).

Data comparison	RMSE (mm)	MB (mm)	$R^2$	$d$
GPS versus radiosonde	4.289	0.157	0.937	0.984
GPS versus AERONET	3.988	1.627	0.904	0.968
AERONET versus radiosonde	2.510	0.062	0.936	0.980
MOD05 versus radiosonde	5.407	0.478	0.843	0.956
MOD05 versus GPS	4.382	1.242	0.912	0.969
MOD05 versus AERONET	4.143	2.170	0.900	0.961
MOD07 versus radiosonde	6.408	1.050	0.808	0.942
MOD07 versus GPS	5.205	1.705	0.900	0.957
MOD07 versus AERONET	5.884	2.908	0.775	0.886

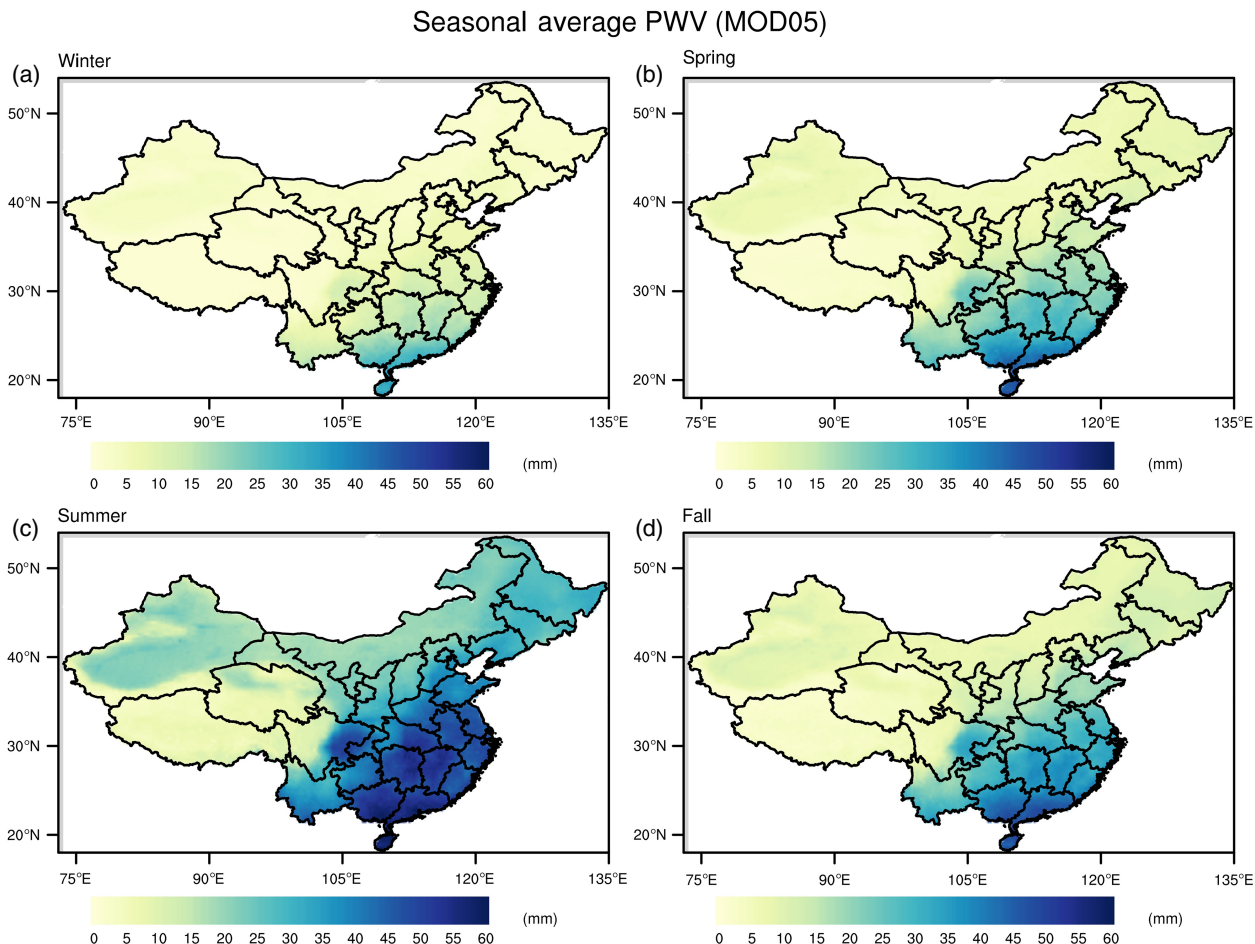


Figure 3. Seasonal averaged PWV over mainland China, using MODIS MOD05 data in (a) winter; (b) spring; (c) summer; and (d) fall; contour lines represent the PWV concentrations.

a few points are significantly biased (Figure 2(a) and Table 2). The comparison between GPS and AERONET data shows good agreement with  $R^2 = 0.904$  and  $d = 0.968$  (Figure 2(b) and Table 2). The mean bias (MB) of GPS data is 0.157 mm with reference to radiosonde and 1.627 mm with reference to AERONET data, indicating GPS data slightly overestimates PWV column. Nonetheless, the spatial distribution of GPS stations in mainland China is more uniform and GPS provides hourly measurements in all weather conditions, which indicates that GPS water vapour data are deemed to be practically feasible for water vapour study in China.

Figure 2(c) presents the scatterplot between radiosonde and AERONET sunphotometer data. A total of 2412 matched data were generated at 10 paired stations for the 12-year period between 2001 and 2012. Results show a good agreement with a high correlation coefficient ( $R^2 = 0.936$ ) and high index of agreement ( $d = 0.980$ ). RMSE is 2.510 mm and MB is 0.062 mm, indicating that very small systematic bias exists. However, AERONET sunphotometer PWV data in mainland China may not be capable for large-scale PWV analysis. First, not all stations provide consistent level 2.0 data between 2001 and 2012. Some stations, such as 'Xinglong' and 'Taihu',

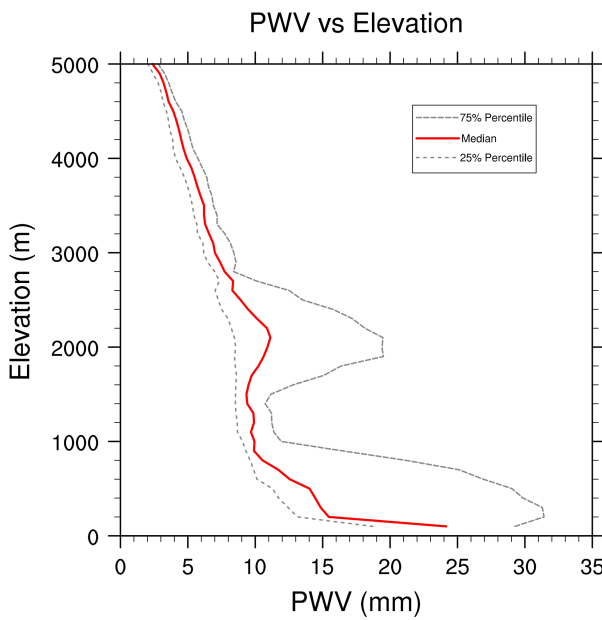


Figure 4. Plot of median, 25 percentile and 75 percentile PWV in different elevations.

have been operated only since 2005. Some other stations such as ‘Dunhuang’, ‘Liangning’, and ‘Nuist’ have been closed since 2001, 2006, and 2011, respectively. Secondly, the AERONET sunphotometer stations in mainland China have an uneven distribution and most of the stations are located in regions such as Beijing, Yangtze River Delta, and Pearl River Delta. In other regions such as Qinghai-Tibet, northwest, and northeast, there are only a few AERONET sunphotometer stations. Thirdly, sunphotometers permit only cloudless and rain-free daytime observations. Therefore, the PWV variability during rainy or night-time periods cannot be observed.

#### 4.3. Validation of MODIS data

MODIS MOD05 and MOD07 water vapour data were compared with radiosonde, GPS, and AERONET sunphotometer, respectively. Spatial averaging was conducted over  $3 \times 3$  pixel window of the site coordinates ( $3 \times 3 \text{ km}^2$  for MOD05 and  $15 \times 15 \text{ km}^2$  for MOD07). Spatial averaging may reduce systematic uncertainty and noise effect (Gao and Kaufman, 2003). GPS and AERONET water vapour data within an hour of MODIS overpass time were also averaged to normalize the time difference.

Comparisons between MOD05 water vapour data and other data sets are illustrated in Figure 2(d)–(f). As PWV retrieval is sensitive to clouds, more than five pixels in a  $3 \times 3$  window, which are deemed as ‘clear’ pixels, would only be selected. Regression between MOD05 and GPS PWV data shows high correlation coefficient ( $R^2 = 0.912$ ) and degree of agreement ( $d = 0.969$ ). Relatively lower correlation coefficient ( $R^2 = 0.843$ ) is observed between MOD05 and radiosonde PWV data, which is mainly caused by the time difference between data sets. The mean bias of MOD05 is unanimously positive when compared with radiosonde, GPS, and AERONET PWV

data, indicating that MOD05 may somehow overestimate the PWV. This overestimation has also been reported in previous studies (Gao and Kaufman, 2003; Prasad and Singh, 2009). The correlation coefficients of MOD07 product are lower than MOD05, and RMSEs of MOD07 are also higher than those of MOD05, as shown in Figure 2(g)–(i) and Table 2. Systematic bias is also calculated in MOD07 products, and the mean bias ranges between 1.050 and 2.908 mm. MOD05 performs better than MOD07 in PWV retrieval, which is in line with previous researches (e.g. Kern *et al.*, 2008; Prasad and Singh, 2009). Three factors may account for the better performance of MOD05. First, Prasad and Singh (2009) show that infrared channels are more sensitive to atmospheric temperature than near infrared channels; however, infrared channels are less sensitive to atmospheric moisture than near infrared channels. Secondly, a better performance of daytime data is observed in MOD07 products (daytime:  $R^2 = 0.894$ ,  $d = 0.956$ ) than night-time data (night-time:  $R^2 = 0.814$ ,  $d = 0.934$ ). Night-time observation may be biased by the time lag between MOD07 and ancillary GDAS (NCEP 1-Degree Global Data Assimilation Model) data, which are used for determining the atmospheric profiles at the lowest level during PWV retrieval (Seemann *et al.*, 2006). Thirdly, MOD05 products have finer resolution than MOD07 products, thus allowing a detailed representation of PWV. In this study, the MOD05 data were also extracted at  $15 \times 15$  pixel-size window, which is at the same size of MOD07. Similar statistical values are observed (regression with GPS data:  $R^2 = 0.909$ , RMSE = 4.403 mm, MB = 1.188 mm,  $d = 0.969$ ), suggesting the window size may not be a control factor for the better performance of MOD05 products.

#### 5. Spatial variation of PWV in mainland China

MODIS products between 2000 and 2012 were used to analyse the spatial distribution of PWV in mainland China. MOD05 products were selected due to their higher spatial resolution and higher accuracy compared with MOD07. Figure 3 shows the spatial variations of PWV in four seasons (winter: December, January and February; spring: March, April and May; summer: June, July and August; fall: September, October and November). Our results show that seasonal variation is pronounced across China, though larger seasonal variation is found over the south and east than that over the north and west, which are consistent with previous studies (Zhai and Eskridge, 1997; Wang and Dian, 2001; Zhao *et al.*, 2012). In the eastern China, increasing PWV contents is associated with decreasing latitudes (Figure 3). In low-latitude coastal areas or islands, high PWV values prevail throughout the entire year ranging from 25 to 55 mm. In mid-latitude areas, the variation of latitude is significantly related to topography. For example, the average PWV over Sichuan Basin is larger than low-lying surrounding areas. In high-latitude northeastern areas, the variation of PWV with latitude is weak.

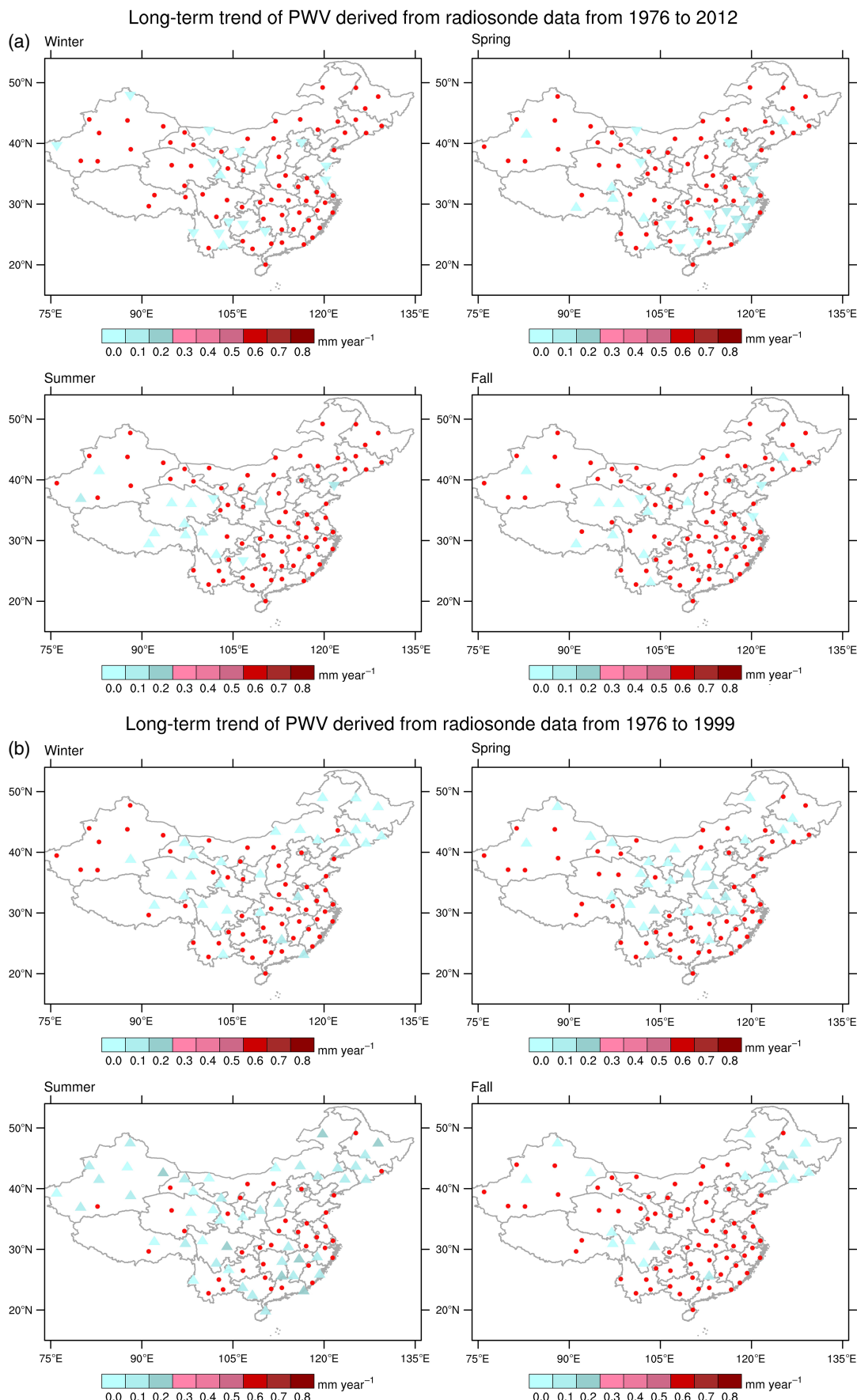


Figure 5. Map of Mann–Kendall test results derived from the radiosonde sites (a) 1976–2012; (b) 1976–1999; and (c) 2000–2012. Sites with confidence level over 95% are filled.

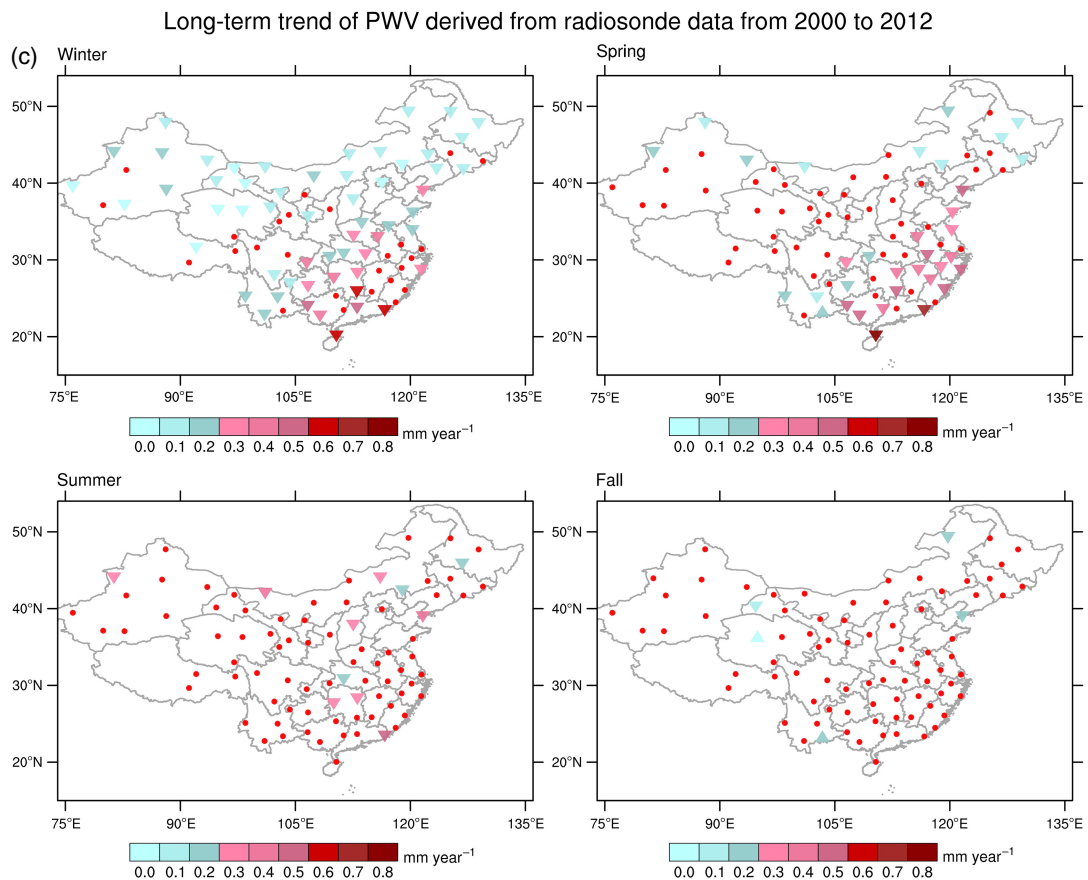


Figure 5. continued.

Table 3. Number of radiosonde sites displaying long-term decreasing/increasing trend.

		Decrease	Increase
1976–1999	Winter	0	29
	Spring	0	29
	Summer	0	46
	Fall	0	18
2000–2012	Winter	57	0
	Spring	33	1
	Summer	11	0
	Fall	3	2
1976–2012	Winter	13	3
	Spring	18	7
	Summer	3	11
	Fall	3	10

In the western China, low PWV values prevail throughout the entire year. PWV column over some areas in the western China is about 7% of that in Hainan Province in winter and 36% in summer. Topography tends to be the dominant factor in the western China. As shown in Figure 4, the median and 25 percentile of annual PWV derived from radiosonde data decrease exponentially with increasing elevation, but the 75 percentile curve shows two peaks at 2000 m and surface level, respectively. That is, the average PWV column is less sensitive to altitude over high PWV regions. For example, the average PWV column over

Yunnan Province is at the same level as in central plain (Figure 4), but the average elevation of Yunnan Province is higher than that of central plain. In contrast, the exponential inverse correlation between PWV and altitude is pronounced over dry regions in western China. For example, in mountainous areas, such as Qilian Mountain (centred at 35°N, 100°E), Tianshan Mountain (42°N, 80°E), lower PWV values are observed, while higher PWV is found in low-altitude areas, such as Junggar Basin (45°N, 85°E).

## 6. Temporal variation of PWV in mainland China

### 6.1. Interannual trend

The Intergovernmental Panel on Climate Change (IPCC) fifth assessment report indicates the unequivocal human-inducing warming trend of climate system (IPCC, 2007). As an important climatic variable, the long-term trend of PWV under the context of climate change is thus of interest. To analyse interannual variation of PWV distribution in mainland China, radiosonde PWV data were selected, which have the longest period of data (between 1976 and 2012). The Mann–Kendall trend test was applied to detect the presence of monotonic trends in all radiosonde sites, which does not require distributional assumptions (Mann, 1945; Kendall, 1975). The Sen's slope estimator was also adopted to quantify the magnitude of upward or downward trends (Sen, 1968). Since

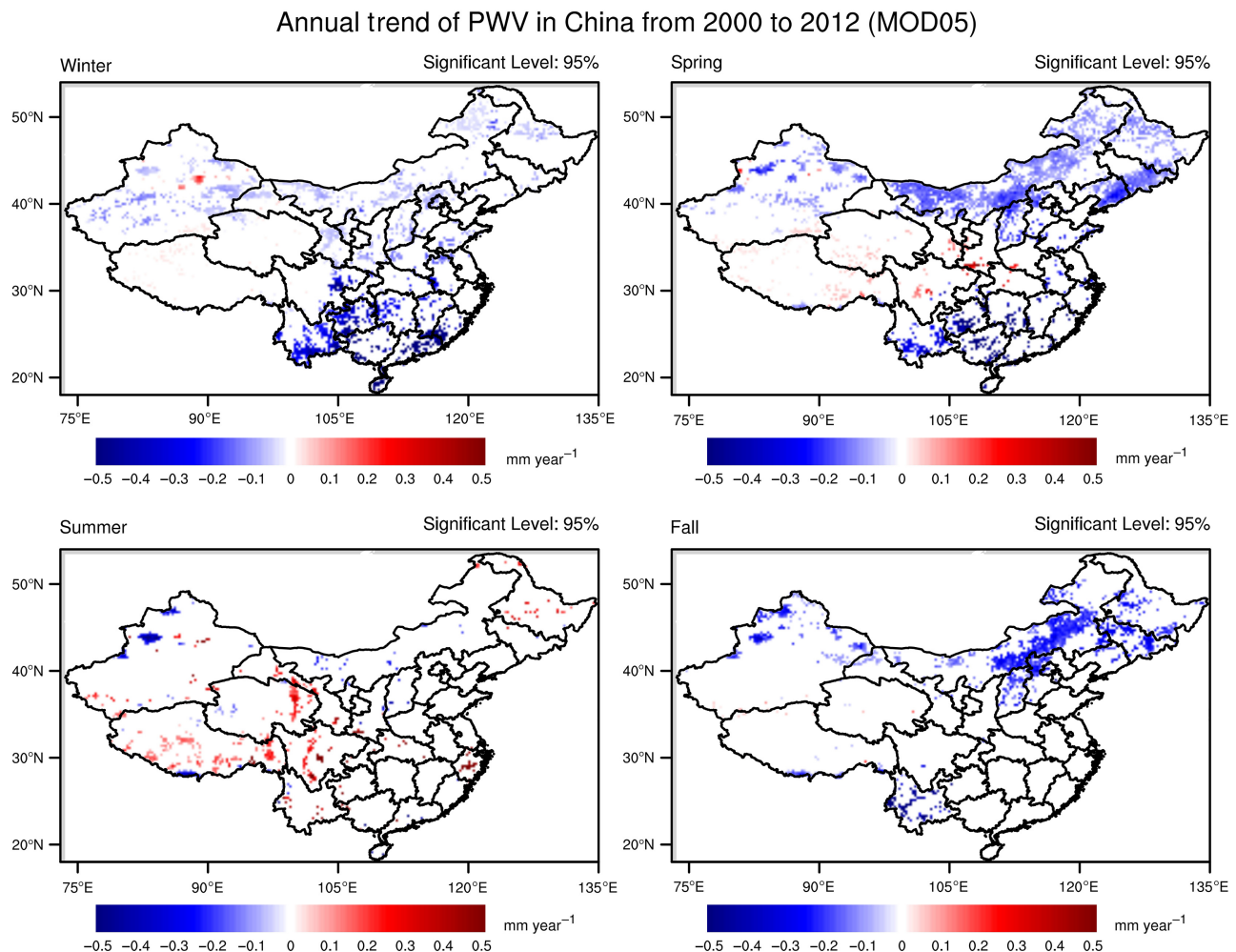


Figure 6. Map of the Sen's slope magnitude derived from the MODIS MOD05 annual averaged data from 2000 to 2012. Areas with confidence level <95% are masked.

seasonal variation was apparent as discussed above, the trend detection test was applied to four seasons.

As shown in Figure 5(a), when the trend test was performed over the entire period (1976–2012), only 16, 25, 14 and 13 of 83 sites displayed significant trends (confidence level: 95%) in four seasons. However, opposite trends are observed over the two periods: 1976–1999 and 1999–2012, respectively (Figure 5(b) and (c)). Among the 83 sites, the numbers of sites with significant increasing trend from 1976 to 1999 are 29, 29, 46, and 18 in winter, spring, summer, and fall, respectively (Figure 5(b) and Table 3). No site shows a decreasing trend in any season during this period. In contrast, a decreasing trend is pronounced in winter and spring throughout China between 1999 and 2012. The numbers of sites with significant decreasing trend from 2000 to 2012 are 57, 33, 11, and 3 in winter, spring, summer, and fall, respectively (Figure 5(c)). Increasing trend is observed in two sites in fall. The trend magnitude ranges from +0.011 to +0.242 mm year<sup>-1</sup> from 1976 to 1999, and -0.842 to +0.227 mm year<sup>-1</sup> from 2000 to 2012. These results indicate that the PWV column in China is not monotonically increasing under the context of global warming. In fact, some parts of China experience

a decreasing PWV in winter and spring in the recent decade.

To extend the spatial trend analysis to other regions that are not close to radiosonde stations, MODIS MOD05 data from 2000 to 2012 were analysed (Figure 6). Results are consistent with the radiosonde observations, decreasing trends are observed over most parts of China in winter, except for Qinghai-Tibet Plateau and Turpan Basin in Xinjiang. The maximum magnitude of decreasing trend over the southern China is about 0.5 mm year<sup>-1</sup>. In spring, decreasing trend is observed over the eastern China, but an increasing trend is found over Qinghai-Tibet Plateau and Loess Plateau. In summer, the increasing trend over Plateau region is more pronounced, but the decreasing trend in the eastern China is diminished. In fall, only a weakened decreasing trend is observed in Xinjiang, Inner Mongolia, Yunnan, and north-eastern China. These results further confirm our observations that the plains region in eastern China experiences dry winter and spring, but the Plateau region in western China experiences wet winter, spring, and summer in the recent decades. Our findings are in line with a recent study on trends of drought across China (Yu *et al.*, 2014).

## 6.2. Weekend effect of PWV

The weekend effect is considered to be an indicator of anthropogenic activities. Some studies confirmed the weekend effect of several meteorological variables, such as DTR, rain frequency, and cloud amount (Ho *et al.*, 2009), but whether PWV displays such weekend effect has not yet been studied. A parametric test was conducted to investigate if there is a significant difference between the PWV at weekends (Friday to Sunday) and weekdays (Monday to Thursday). First, PWV data of each week were converted to anomalies by subtracting the weekly difference. The difference between weekend anomalies and weekday anomalies were then calculated for each GPS and radiosonde site in weekly basis. The anomaly difference between two groups of randomly classified PWV data for each week was also calculated. A *t*-test was applied to evaluate if there is a statistically significant difference between two data sets. The averaged differences between weekday and weekend are shown in Figure 7(a) and (b). The sites with statistically significant *t*-test results (>95%) were denoted as solid triangles. Most of the radiosonde sites over the eastern China show negative difference between weekends and weekdays. Over western China, where human activities are less intense, such difference is insignificant. As shown in Figure 7(b), 10 out of 22 GPS stations show negative differences (four stations were discarded due to insufficient data). These results imply that water vapour contents may increase during weekdays when human activities are more intense. The low PWV values during weekends may be correlated with the reduction of methane emission, an important source of water vapour in the upper atmosphere (Jacobson, 2012).

## 6.3. Diurnal cycle of PWV

The diurnal cycle of PWV over China was analysed using hourly GPS PWV data based on harmonic analysis. Hourly GPS PWV data were first converted to daily anomalies by subtracting daily average PWV of each day. Those days with more than one-third of missing values were not calculated. Secondly, the daily anomalies of each station were averaged over four seasons between 1999 and 2009. Thirdly, the average diurnal anomalies of each station were decomposed spectrally using Fourier transform equation. The phase, amplitude, and percent of variance of the first harmonic were calculated for each station in four seasons. The averaged PWV can then be computed using Equation (12):

$$\text{PWV}(t) = \text{PWV}(0) + A \cos \left[ \frac{2\pi}{24} (t - \sigma) \right] + R \quad (12)$$

where  $\text{PWV}(0)$  is the daily mean value,  $R$  is the residual,  $A$  is the diurnal amplitude, and  $\sigma$  is the phase, which corresponds to the UTC time of considered maximum PWV.

The resulting phase and amplitude are presented in vectors, and arrows are coloured based on the percent variance that can be explained by the first harmonic (Figure 8). The revealed diurnal cycle is pronounced in summer (June–July–August), spring (March–April–May), and

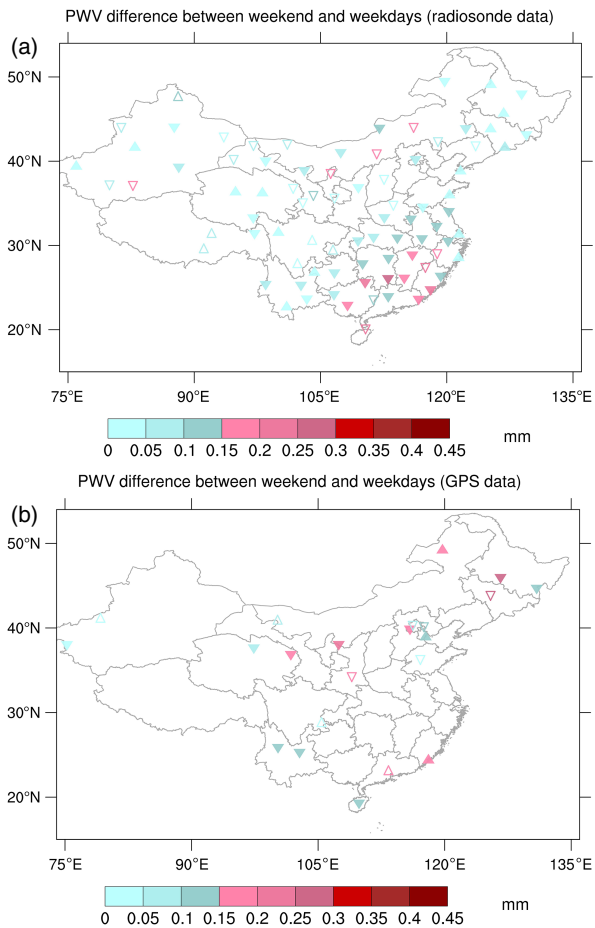


Figure 7. PWV difference between weekends and weekdays. Sites with confidence level over 95% are filled.

fall (September–October–November), but weak in winter (December–January–February). The diurnal cycle explains over 50% sub-daily variance in 21, 20, 17, and 4 of 26 GPS sites in summer, spring, fall, and winter, respectively. Among those sites where the percent variance of the 24-h cycle is over 50%, the magnitude ranges from 0.18 mm ('HRBN' in Heilongjiang) to 1.44 mm ('LUZH' in Sichuan) in spring, 0.13 mm ('CHUN' in Jilin) to 1.98 mm ('QION' in Hainan) in summer, and 0.14 mm ('HLAR' in Inner Mongolia) to 1.14 mm ('QION' in Hainan) in fall. In winter, the magnitude of diurnal cycle is small (<0.5 mm) in most sites, except for sites 'QION' (0.61 mm) and 'LUZH' (1.03 mm). The spatial patterns of amplitude are similar in summer, spring, and fall: the lowest amplitude is unanimously found in the northeast China, while the highest amplitude is found in Sichuan and Hainan Provinces where the humidity is high. It is also noted some sites over the western China show larger amplitude of diurnal cycle than the east, though the west is drier than the east (Figure 3). The large temperature difference may account for the apparent diurnal cycle over the west. The phase, which corresponds to time with peak PWV, varies among different stations. The difference in phase among summer, spring, and fall is small (<2.5 h) in all sites with pronounced diurnal cycle (percent variance > 50% in three seasons), indicating the peak time

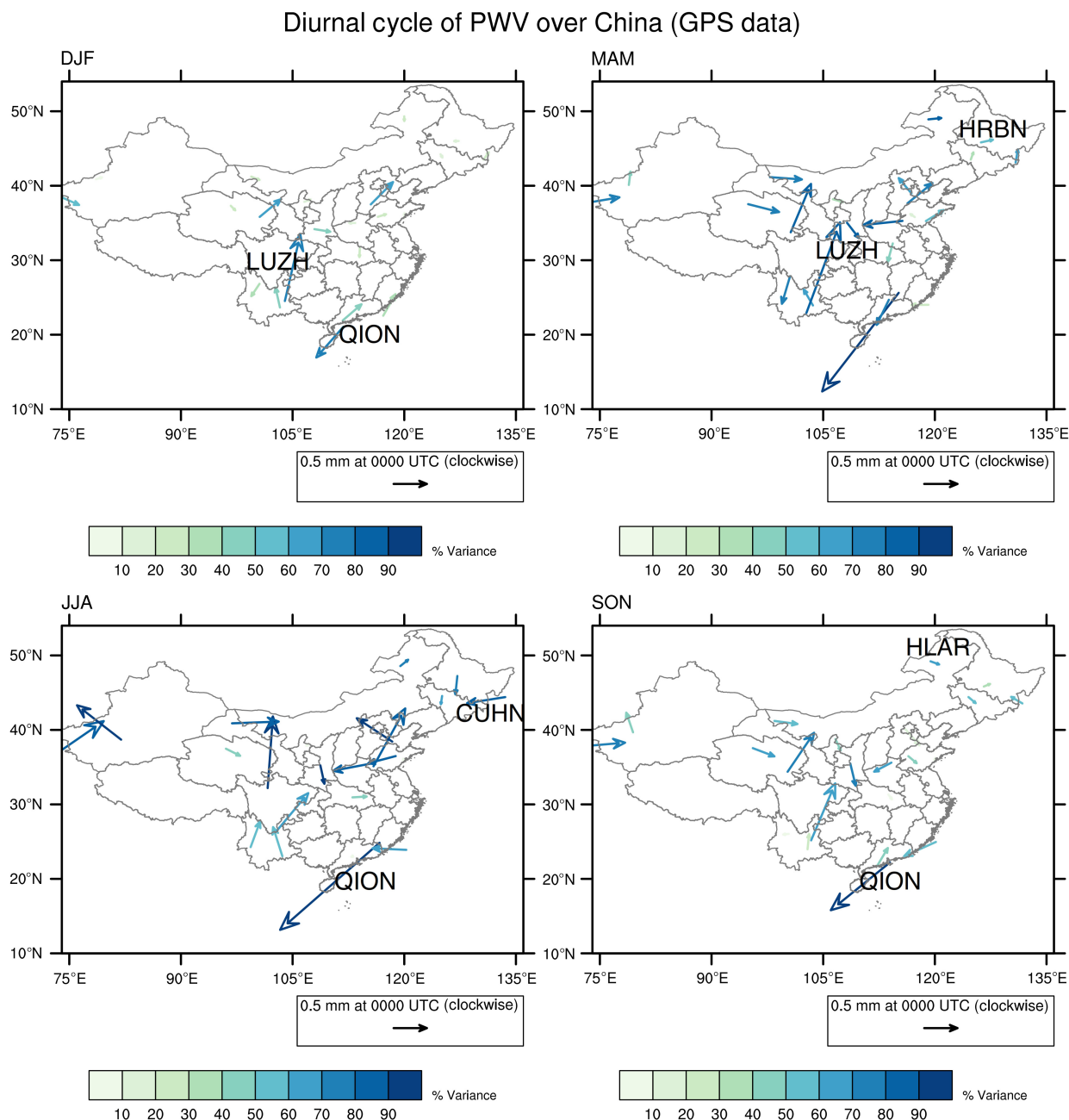


Figure 8. Results of Fourier transform over mainland China in four seasons. Length of vector represents the amplitude of diurnal cycle. Direction represents the phase of diurnal cycle. Colour of the vector represents the variance that can be derived from the first harmonic.

does not change much with seasons. The peaks of PWV are observed in the noon or the early afternoon (1100 LST to 1500 LST) in the central China. In southern China, the peaks of PWV always occur in the afternoon (1200 LST to 1600 LST). In the sites of the northwestern China, the peaks of PWV occurred in the morning time (0600 to 1000 LST). Several atmospheric processes, including surface evapotranspiration, moisture convergence, and precipitation, may affect the diurnal variation of PWV in China (Dai *et al.*, 2002). During the day, surface evapotranspiration accumulates water vapour and latent heat in the lower troposphere before convection occurs, which explains that the peaks of PWV are observed in the afternoon in some sites. For other sites where PWV peaks in the evening or

in the morning, the impact of precipitation dominates. Yu *et al.* (2007) suggest summer precipitation maxima at midnight over western China. This is consistent with the PWV peaks at midnight, as precipitation can moisten the lower atmosphere. In addition, diurnal changes in wind direction may also lead to diurnal variations of PWV. The wind from the sea brings water to inland areas, while the wind arising from inland takes water away (Dai *et al.*, 2002).

## 7. Conclusion

In this study, a comprehensive analysis of PWV data using a multi-sensor approach was undertaken in mainland

China. With reference to radiosonde data, GPS and AERONET sunphotometer water vapour data were found to have higher accuracy than MODIS satellite data. Our comparison results also confirmed that MOD05 products outperformed MOD07.

Thirteen years of MODIS MOD05 products were investigated to analyse the spatial variation of PWV in China. Increasing PWV content was generally associated with decreasing latitude in the eastern part of China, which was related to the temperature gradient. As for western China, where the average PWV was low, altitude tends to be a dominant factor in PWV variation.

Temporal variations of PWV distribution in mainland China were investigated. The interannual variation of PWV was analysed based on radiosonde data using the Mann–Kendall test. A monotonic increasing trend was found in more than half of the sites in summer from 1976 to 1999, but an opposite decreasing trend was found from 2000 to 2012, especially during winter. The decreasing trend was also shown by MODIS products across the eastern China. The decreasing trend might be attributed to the increasing frequency of drought.

In addition, it was shown that the averaged PWV in weekends was lower than weekdays, which may be correlated to lower methane emissions during weekends. The diurnal cycle was investigated using Fourier transform. It was shown that the 24-h cycle could explain more than 50% of the sub-daily variance in most sites, in all seasons except for winter. Large diurnal amplitude was found in some sites in western China, which might result from the large DTR over the region. The phase of diurnal cycle varied with stations but did not change much in relation to seasons. Several reasons including surface evapotranspiration, precipitation, and wind direction might account for diurnal variation.

In conclusion, spatial and temporal analysis of precipitation water vapour indicates spatial and temporal variation in climatic relationships as well as anthropogenic activities in mainland China. These features indicate more complex climatological controls in meteorological and hydrographical processes from a regional-scale weather system to a global climate system. The maps and analysis presented here provide additional contexts for the application of precipitable water vapour studies in meteorology, climatology, hydrology, and ecology research fields. Future work on the integration of ground-based, space-based PWV data, and numerical weather prediction systems (e.g. NHM and WRF model) will be conducted for improving both short-term prediction of regional-scale weather system and long-term climate change. In addition, more analysis on the complex relationships between PWV, surface temperature, and precipitation will be undertaken in the near future.

## Acknowledgements

This research was sponsored by the grants PolyU 1-ZVAJ from the Faculty of Construction and Environment, the Hong Kong Polytechnic University, the grants PolyU

1-ZVBP, PolyU 1-ZVBR from the Research Institute for Sustainable Urban Development, the Hong Kong Polytechnic University, and grant PolyU 5217/11E (B3-Q28F) from the Hong Kong Research Grants Council. Zhizhao Liu thanks the supports of the Program of Introducing Talents of Discipline to Universities (Wuhan University, GNSS Research Center), China. The authors thank the NASA Goddard Space Flight Center for the MODIS images, Brent Holben from NASA for AERONET data, observatories in China for radiosonde data. Shirong Ye and Peng Jiang from Wuhan University, China are acknowledged for providing the GPS-derived water vapour data.

## References

- Alexandrov MD, Schmid B, Turner DD, Cairns B, Oinas V, Lacis AA, Gutman SI, Westwater ER, Smirnov A, Eilers J. 2009. Columnar water vapor retrievals from multifilter rotating shadowband radiometer data. *J. Geophys. Res. Atmos.* **114**: D02306, doi: 10.1029/2008JD010543.
- Bevis M, Businger S, Herring TA, Rocken C, Anthes RA, Ware RH. 1992. GPS meteorology: remote sensing of atmospheric water vapor using the global positioning system. *J. Geophys. Res.* **97**: 15787–15801.
- Bi Y, Mao J, Wang M, Li C. 2004. Remote sensing of atmospheric water vapor in the region of southwest China using GPS. *Proc. SPIE* **5832**: 551–562.
- Bokoye AI, Royer A, O'Neill NT, Cliché P, McArthur LJB, Teillet PM, Fedosejevs G, Thériault J-M. 2003. Multi-sensor analysis of integrated atmospheric water vapor over Canada and Alaska. *J. Geophys. Res.* **108**(D15): 4480, doi: 10.1029/2002JD002721.
- Bokoye AI, Royer A, Cliché P, O'Neill NT. 2007. Calibration of sun radiometer-based atmospheric water vapor retrievals using GPS meteorology. *J. Atmos. Oceanic Technol.* **24**: 964–979.
- Brette MJ, Galvin JFP. 2003. Back to basics: radiosondes: Part 1 – the instrument. *Weather* **58**: 336–341.
- China Census Data. 2010. National Bureau of Statistics of China. <http://www.stats.gov.cn/english/> (accessed 29 September 2014).
- Collins P, Mireault Y, Héroux P. 2002. Strategies for estimating tropospheric delays with GPS. In *Proceedings of 2002 IEEE Position Location and Navigation Symposium*, Palm Springs, CA, 15–18 April 2002.
- Dai A, Wang J, Ware RH, Van Hove T. 2002. Diurnal variation in water vapor over North America and its implications for sampling errors in radiosonde humidity. *J. Geophys. Res. Atmos.* **107**(D10): 4090, doi: 10.1029/2001JD000642.
- Elgered G, Johansson L, Rönnäng B, Davis J. 1997. Measuring regional atmospheric water vapor using the Swedish permanent GPS network. *Geophys. Res. Lett.* **24**: 2663–2666.
- Emardson TR, Elgered G, Johansson JM. 1998. Three months of continuous monitoring of atmospheric water vapor with a network of GPS receivers. *J. Geophys. Res.* **103**: 1807–1820.
- Fontaine B, Roucou P, Trzaska S. 2003. Atmospheric water cycle and moisture fluxes in the West African monsoon: mean annual cycles and relationship using NCEP/NCAR reanalysis. *Geophys. Res. Lett.* **30**: 1117, doi: 10.1029/2002GL015834.
- Gaffen D, Barnett T, Elliott W. 1991. Space and time scales of global tropospheric moisture. *J. Clim.* **4**(10): 989–1008.
- Gao BC, Kaufman YJ. 1998. MODIS near-IR water vapor algorithm theoretical basis document. ATBD-MOD-05, NASA Goddard Space Flight Center: Greenbelt, MD.
- Gao BC, Kaufman YJ. 2003. Water vapor retrievals using moderate resolution imaging spectroradiometer (MODIS) near-infrared channels. *J. Geophys. Res.* **108**(D13): 4389, doi: 10.1029/2002JD003023.
- Halthore RN, Eck TF, Holben BN, Markham BL. 1997. Sun photometric measurements of atmospheric water vapor column abundance in the 940-nm band. *J. Geophys. Res.* **102**: 4343–4352.
- Held IM, Soden BJ. 2000. Water vapor feedback and global warming 1. *Annu. Rev. Energy Environ.* **25**(1): 441–475.
- Hernández-Pajares M, Juan JM, Sanz J, Colombo OL, van der Marel H. 2001. A new strategy for real-time integrated water vapor determination in WADGPS networks. *Geophys. Res. Lett.* **28**: 3267–3270.

- Ho CH, Choi YS, Hur SK. 2009. Long-term changes in summer weekend effect over northeastern China and the connection with regional warming. *Geophys. Res. Lett.* **36**(15): 15706.
- Holben BN, Eck TF, Slutsker I, Tanré D, Buis JP, Setzer A, Vermote E, Reagan JA, Kaufman Y, Nakajima T, Lavenu F, Jankowiak I, Smirnov V. 1998. AERONET – a federated instrument network and data archive for aerosol characterization. *Remote Sens. Environ.* **66**: 1–16.
- Intergovernmental Panel on Climate Change (IPCC) Working Group I. 2007. *Climate Change 2007: The Physical Science Basis*, Manning M, Qin D (eds). Cambridge University Press: New York, NY.
- Iwabuchi T, Naito I, Mannouji N. 2000. A comparison of global positioning system retrieved precipitable water vapor with the numerical weather prediction analysis data over the Japanese Islands. *J. Geophys. Res.* **105**: 4573–4585.
- Jacobson M. 2012. *Air Pollution and Global Warming: History, Science and Solutions*, 2nd edn. Cambridge University Press: Cambridge, UK.
- Jin S, Li Z, Cho J. 2008. Integrated water vapor field and multiscale variations over China from GPS measurements. *J. Appl. Meteorol. Climatol.* **47**(11): 3008–3015.
- Kaufman YJ, Gao BC. 1992. Remote sensing of water vapor in the near IR from EOS/MODIS. *IEEE Trans. Geosci. Remote Sens.* **30**: 871–884.
- Kendall MG. 1975. *Rank Correlation Methods*. Charles Griffin: London.
- Kern A, Bartholy J, Borbás ÉE, Barcza Z, Pongrácz R, Ferencz C. 2008. Estimation of vertically integrated water vapor in Hungary using MODIS imagery. *Adv. Space Res.* **41**(11): 1933–1945.
- King MD, Kaufman YJ, Menzel WP, Tanre D. 1992. Remote sensing of cloud, aerosol, and water vapor properties from the moderate resolution imaging spectrometer (MODIS). *IEEE Trans. Geosci. Remote Sens.* **30**: 1–27.
- Li Z. 2003. Comparison of precipitable water vapor derived from radiosonde, GPS, and moderate-resolution imaging spectroradiometer measurements. *J. Geophys. Res. Atmos.* **108**(D20): 4651, doi: 10.1029/2003JD003372.
- Liu Z, Wong MS, Nichol J, Chan PW. 2012. A multi-sensor study of water vapour from radiosonde, MODIS and AERONET: a case study of Hong Kong. *Int. J. Climatol.* **2012**: 31, doi: 10.1002/joc.3412.
- Mann HB. 1945. Nonparametric tests against trend. *Econometrica* **13**: 245–259.
- Mätzler C, Martin L, Guerova G, Ingold T. 2002. Assessment of integrated water vapor data at Bern from GPS, sun photometry, microwave radiometry and radiosonde. In *Proceedings of 2nd Workshop of COST Action 716, Exploitation of Ground-Based GPS for Meteorology*, GFZ Potsdam, Germany, 28–29 January 2002.
- Menzel WP, Gumley LE. 1996. MODIS atmospheric profile retrieval algorithm theoretical basis document. ATBD-MOD-07, NASA Goddard Space Flight Center, Greenbelt, MD, 32 pp.
- Miloshevich LM, Vömel H, Whiteman DN, Lesht BM, Schmidlin FJ, Russo F. 2006. Absolute accuracy of water vapor measurements from six operational radiosonde types launched during AWEX-G and implications for AIRS validation. *J. Geophys. Res. Atmos.* **111**: D09S10, doi: 10.1029/2005JD006083.
- Niell AE, Coster AJ, Solheim FS, Mendes VB, Toor PC, Langley RB, Upham CA. 2001. Comparison of measurements of atmospheric wet delay by radiosonde, water vapor radiometer, GPS, and VLBI. *J. Atmos. Oceanic Technol.* **18**: 830–850.
- Pérez-Ramírez RD, Whiteman DN, Smirnov A, Lyamani H, Holben BN, Pinker R, Andrade M, Alados Arboledas L. 2014. Evaluation of AERONET precipitable water vapor versus microwave radiometry, GPS and radiosondes at ARM sites. *J. Geophys. Res. Atmos.* **119**(15): 9596–9613, doi: 10.1002/2014JD021730.
- Piao S, Ciais P, Huang Y, Shen Z, Peng S, Li J, Zhou L, Liu H, Ma Y, Ding Y, Friedlingstein P, Liu C, Tan K, Yu Y, Zhang T, Fang J. 2010. The impacts of climate change on water resources and agriculture in China. *Nature* **467**(2): 43–51.
- Prasad AK, Singh RP. 2009. Validation of MODIS Terra, AIRS, NCEP/DOE AMIP-II reanalysis-2, and AERONET Sun photometer derived integrated precipitable water vapor using ground-based GPS receivers over India. *J. Geophys. Res. Atmos.* **114**: D05107, doi: 10.1029/2008JD011230.
- Raval A, Ramanathan V. 1989. Observational determination of the greenhouse effect. *Nature* **342**(6251): 758–761.
- Reagan JA, Thome KJ, Herman BM. 1992. A simple instrument and technique for measuring columnar water vapor via near-IR differential solar transmission measurements. *IEEE Trans. Geosci. Remote Sens.* **30**(4): 825–831.
- Schmid B, Thome KJ, Demoulis P, Peter R, Matzler C, Sekler J. 1996. Comparison of modeled and empirical approaches for retrieving columnar water vapor from solar transmittance measurements in the 0.94 mm region. *J. Geophys. Res.* **101**: 9345–9358.
- Seemann SW, Borbas EE, Li J, Menzel WP, Gumley LE. 2006. MODIS atmospheric profile retrieval algorithm theoretical basis document. ATBD-MOD-07, NASA Goddard Space Flight Center: Greenbelt, MD.
- Sen PK. 1968. Estimates of the regression coefficient based on Kendall's Tau. *J. Am. Stat. Assoc.* **63**(324): 1379–1389.
- Soden BJ, Lanzante JR. 1996. An assessment of satellite and radiosonde climatologies of upper-tropospheric water vapor. *J. Clim.* **9**(6): 1235–1250.
- Song S, Zhu W, Ding J, Peng J. 2006. 3D water-vapor tomography with Shanghai GPS network to improve forecasted moisture field. *Chin. Sci. Bull.* **51**(5): 607–614.
- Starr DO'C, Melfi S (eds). 1991. *The Role of Water Vapor in Climate. A Strategic Research Plan for the Proposed GEWEX Water Vapor Project (GVaP)*. University of California Libraries: Davis, CA.
- Tregoning P, Boers R, O'Brien D, Hendy M. 1998. Accuracy of absolute precipitable water vapor estimates from GPS observations. *J. Geophys. Res.* **103**: 28701–28710.
- Turner DD, Lesht BM, Clough SA, Liljegegren JC, Revercomb HE, Tobin DC. 2003. Dry bias and variability in Vaisala RS80-H radiosondes: the ARM experience. *J. Atmos. Oceanic Technol.* **20**(1): 117–132, doi: 10.1175/1520-0426(2003)020<0117:DBAVIV>2.0.CO;2.
- Van Baelen J, Aubagnac JP, Dabas A. 2005. Comparison of near-real time estimates of integrated water vapor derived with GPS, radiosondes, and microwave radiometer. *J. Atmos. Oceanic Technol.* **22**(2): 201–210.
- Wang H, Chen H. 2012. Climate control for southeastern China moisture and precipitation: Indian or East Asian monsoon? *J. Geophys. Res.* **117**(D12): D12109.
- Wang XL, Dian JG. 2001. Late-twentieth-century climatology and trends of surface humidity and temperature in China. *J. Clim.* **14**(13): 2833–2846.
- Willmott CJ. 1981. On the validation of models. *Phys. Geogr.* **2**: 184–194.
- World Meteorological Organization. 2008. Guide to Meteorological Instruments and Methods of Observation. World Meteorological Organization: Geneva, Switzerland.
- Yu RC, Zhou TJ, Xiong AY, Zhu YJ, Li JM. 2007. Diurnal variations of summer precipitation over contiguous China. *Geophys. Res. Lett.* **34**: L01704, doi: 10.1029/2006GL028129.
- Yu M, Li Q, Hayes MJ, Svoboda MD, Heim RR. 2014. Are droughts becoming more frequent or severe in China based on the Standardized Precipitation Evapotranspiration Index: 1951–2010? *Int. J. Climatol.* **34**: 545–558, doi: 10.1002/joc.3701.
- Zhai PM, Eskridge RE. 1997. Atmospheric water vapor over China. *J. Clim.* **10**: 2643–2652.
- Zhao T, Dai A, Wang J. 2012. Trends in tropospheric humidity from 1970 to 2008 over China from a homogenized radiosonde dataset. *J. Clim.* **25**(13): 4549–4567.